Constraints and detection capabilities of GW polarizations with space-based detectors in different TDI combinations

Jie Wu (吴洁) [ID] , Mengfei Sun (孙孟飞) [ID] , and Jin Li (李瑾) [ID] *

College of Physics, Chongqing University, Chongqing 401331, China and
Department of Physics and Chongqing Key Laboratory for Strongly Coupled Physics,
Chongqing University, Chongqing 401331, China

Time-delay interferometry (TDI) is essential in space-based gravitational wave (GW) detectors, effectively reducing laser noise and improving detection precision. As one of the most promising GW detectors, the space-based detectors are able to observe the effects from GW polarizations. The detection of GW additional polarizations carries significant implications, potentially revealing deviations from general relativity and opening avenues to explore alternative gravity theories. In this study, we examine the impacts of second-generation TDI combinations on GW polarization detection by simulating LISA, Taiji, and TianQin, including realistic orbital effects such as link length and angle variations. The detector performance is assessed through sensitivity curves derived from averaged response functions, as well as signal-to-noise ratio (SNR) of binary black holes (BBHs). For massive BBHs, the $\mathcal{A}$ and $\mathcal{E}$ channels typically offer the best sensitivity, while the X channel in TianQin is most effective for detecting additional polarizations. For stellar-mass BBHs, the α channel provides the highest SNR for vector modes in LISA and Taiji specifically for lower-mass systems, while the $\mathcal{A}$ and $\mathcal{E}$ channels are optimal for higher masses or other polarizations. TianQin consistently favors the X channel for additional polarizations. Our findings emphasize the importance of selecting high-sensitivity TDI combinations to enhance detection capabilities across different polarizations, deepening our insight into GW sources and the fundamental nature of spacetime.

I. INTRODUCTION

The first direct detection of gravitational waves (GWs) was made by LIGO and Vrigo Collaborations in 2015, opening a new window for testing general relativity (GR) and exploring gravity in strong fields [1]. One way to test GR and constraint alternative gravity theories is to search for deviations from GR in GW observations [2]. Currently, almost 100 GW events have been detected, with no evidence of new physics beyond GR [3–5]. Ground-based detectors like LIGO, Virgo, and KAGRA can only detect frequency bands higher than 10Hz due to their arm length limitations [6–8]. There are plentiful sources in the low-frequency band, which facilitates more rigorous testing of GR [9]. Constructing a space-based detector with an arm length of millions of kilometers in space can effectively detect low-frequency sources [10]. The proposed space-based GW detection missions, such as LISA [11], Taiji [12], and TianQin [13], are designed to operate within a sensitive frequency band of millihertz, while DECIGO [14], ALIA [15], and BBO [16] are intended to cover a sensitive frequency band ranging from 0.1 to 10 Hz.

GW detection utilizes laser interferometry technology by precisely measuring the phase changes in the laser's round-trip propagation to capture GW signals. Ground-based detectors can eliminate the laser frequency noise by establishing precise interferometric arms. On the contrary, the arms of space-based detector change with time because orbital dynamics leads to variations in the distance between spacecraft (S/C). Consequently, the laser frequency noise is several orders of magnitude higher than other noise, and it must be removed from the data to achieve GW sensitivity [17]. To suppress laser frequency noise, Tinto *et al.* introduced time-delay interferometry (TDI), which constructs a virtual equal-arm interferometer by combining delayed scientific data streams [18]. The combination of TDI can be solved mathematically based on the relevant theories of algebraic geometry [19]. In reality, there might be a situation where one of the arms is damaged and data is missing, thereby resulting in the research and development of other combinations [20].

Some recent studies have discussed the TDI combination and GW polarization. Wu *et al.* generalized the combinatorial algebraic approach to construct various classes of modified second-generation TDI solutions [21]. Zhang *et al.* provided an analytical formula for the average polarization response function in different TDI combinations and obtained their asymptotic behaviors [19]. Wang *et al.* analytically evaluate the response functions for arbitrary TDI combinations while enumerating all possible polarizations [22]. In Ref. [23], Wang *et al.* used numerical methods to evaluate the noise level and sensitivity of different TDI channels. These studies have provided valuable research directions and foundational insights for exploring GW polarizations. Most of these studies focus either on theoretically deriving analytical or semi-analytical responses and sensitivities across different polarizations, or on numerically simulating tensor modes in various TDI combinations. Few have considered the scenario of simulating various space-based detectors probing different polarizations across diverse TDI com-

arXiv:2411.03631v1 [gr-qc] 6 Nov 2024

binations.

We conduct further in-depth research using numerical simulations to study the noise and response of different polarizations in different TDI combinations. We separately simulate the different TDI combinations of the three detectors, LISA, Taiji, and TianQin. Meanwhile, continuing the previous work [24, 25], we investigate the scenarios of detecting massive black hole binaries (MBHBs) and stellar-mass binary black holes (SBBHs) using different TDI combinations, presenting the best combinations for different masses. Employing the stochastic gravitational wave background (SGWB) with a flat spectrum to simulate the GW responses across the entire frequency band, we compute the sensitivity curves of different TDI combinations and evaluated the corresponding detection capabilities. Through the systematic investigation, we analyze the constraints on GW polarization and the detection performance from multiple perspectives.

This paper is organized as follows. In Sec. II, we present the waveforms of binary black holes (BBHs) and flat spectrum SGWB. In Sec. III, we review the relevant aspects of the detector, including the orbit configuration, response, TDI, noise, and sensitivity. In Sec. IV, we explain the approach for calculating the signal-to-noise ratio (SNR) and the procedural steps of the simulation. In Sec. V, we present simulation results for different TDI combinations and analyze the best combinations under various scenarios. Finally, we summarize the results of our research in Sec. VI. Throughout this paper, we use units with $G = c = 1$, where G is the gravitational constant and c is the speed of light.

II. GW SIGNAL

In general, GWs have six polarizations: two tensor modes ($+$ and $\times$), two vector modes (X and Y) and two scalar modes (B and L) [26]. The GWs with six polarizations can be expressed in tensor form:

$$h_{ij} = \sum_A h_A e_{ij}^A, \tag{1}$$

where $A = \{+, \times, X, Y, B, L\}$ represents for the six polarizations, h_A are the waveforms, and e^A are the polarization tensors in the source frame.

According to Ref. [27], we construct the solar system barycenter (SSB) frame, as shown in Fig. 1. For GWs propagating along the $\hat{k}$, we can define the following right-handed orthonormal basis:

$$\begin{aligned} \hat{u} &= [\sin\lambda, -\cos\lambda, 0], \\ \hat{v} &= [-\sin\beta\cos\lambda, -\sin\beta\sin\lambda, \cos\beta], \\ \hat{k} &= [-\cos\beta\cos\lambda, -\sin\lambda\cos\beta, -\sin\beta], \end{aligned} \tag{2}$$

where (λ, β) are ecliptic coordinates of the GW source. The source frame can be transformed to the SSB frame via the polarization angle ψ. The polarization tensors e^A
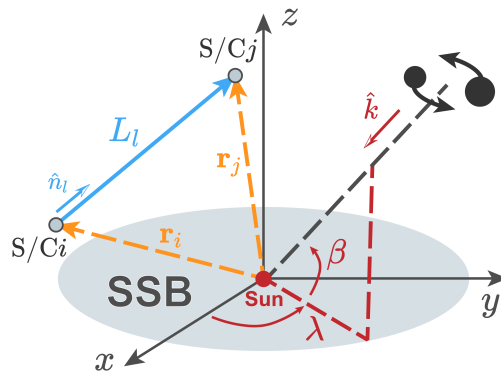

FIG. 1. The diagram of the SSB frame. In the SSB frame, the z-axis is is parallel to the orbital angular momentum of the Earth, while the x-axis points to the vernal equinox.

in the source frame can be expressed using the polarization tensors ϵ^A in the SSB frame [26–28]:

$$\begin{aligned} e^+ &= \epsilon^+ \cos 2\psi + \epsilon^\times \sin 2\psi, \\ e^\times &= -\epsilon^+ \sin 2\psi + \epsilon^\times \cos 2\psi, \\ e^X &= \epsilon^X \cos\psi + \epsilon^Y \sin\psi, \\ e^Y &= -\epsilon^X \sin\psi + \epsilon^Y \cos\psi, \\ e^B &= \epsilon^B, \\ e^L &= \epsilon^L, \end{aligned} \tag{3}$$

with

$$\begin{aligned} \epsilon^+ &= \hat{u} \otimes \hat{u} - \hat{v} \otimes \hat{v}, \\ \epsilon^\times &= \hat{u} \otimes \hat{v} + \hat{v} \otimes \hat{u}, \\ \epsilon^X &= \hat{u} \otimes \hat{k} + \hat{k} \otimes \hat{u}, \\ \epsilon^Y &= \hat{v} \otimes \hat{k} + \hat{k} \otimes \hat{v}, \\ \epsilon^B &= \hat{u} \otimes \hat{u} + \hat{v} \otimes \hat{v}, \\ \epsilon^L &= \hat{k} \otimes \hat{k}. \end{aligned} \tag{4}$$

For the waveform of BBH, we adopt Eqs. (2)∼(5) from Ref. [24] to stimulate three typical-mass MBHBs and two SBBHs. Among them, the duration of MBHBs are set to 90 days before reaching the innermost stable circular orbit, while those of SBBHs are set to one year before reaching 1 Hz. Through the parameterized post-Einstein (ppE) framework, the model-independent waveforms are numerically calculated.

For the purpose of calculating the GW average response and sensitivity curves, a flat power spectral density (PSD) of the SGWB is introduced here. Such an isotropic flat SGWB is equivalent to white noise covering all frequencies at once [30]. As depicted in Fig. 3, the time-domain signal is generated by employing the PSD in the frequency domain and adding random phase information. In the subsequent computations, the SGWB corresponding to the six polarizations are all generated. We will elaborate on this in detail in Sec. III C.
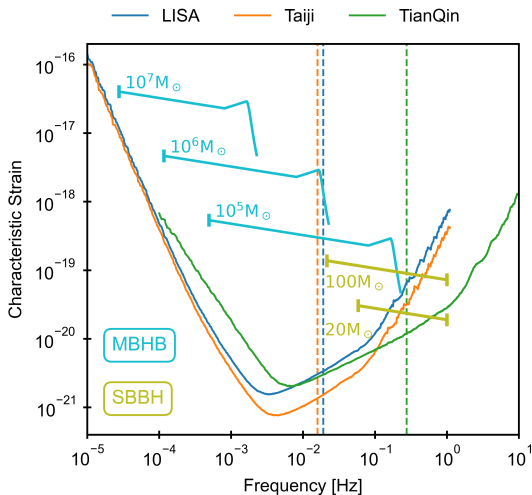
FIG. 2. Selected BBHs and sensitivity curves. The vertical axis represents the dimensionless characteristic strain $\sqrt{fS_n(f)}$. The BBH curve is derived from Ref. [29] and is intended solely for illustrative purposes. For luminosity distance, we set SBBH at $D_L = 44.6$ Mpc and MBHB at $D_L = 6.79$ Gpc. The three vertical dashed lines represent the transfer frequencies of the three space-based detectors.

III. DETECTOR

A. Detector orbit and response

The millihertz space-based GW detectors, LISA, Taiji, and TianQin, are all composed of three S/C, forming a nearly equilateral triangle. LISA and Taiji adopt heliocentric orbits, trailing/leading the Earth by approximately 20 degrees with a period of one year [11, 12]. TianQin employs a geocentric orbit, and the normal direction of the detector plane always points towards the reference source RX J0806.3+1527 [13]. The arm lengths L of the detectors are 2.5×10^6 km (LISA), 3×10^6 km (Taiji), and $\sqrt{3} \times 10^5$ km (TianQin), respectively.

The motion of the S/C can be described by the Keplerian orbit. In the SSB frame, the position vector of the i-th S/C is $\mathbf{r}_i = (x_i, y_i, z_i)$. For the heliocentric and geocentric orbits, the analytical components of $\mathbf{r}_i$ as a function of time are provided in Refs. [31, 32]. We employ the Keplerian orbit expanded to the order of e^2, where e is the orbital eccentricity.

The Michelson interferometer detects GWs by measuring the relative changes in the lengths of its two arms. The change in length of one arm induced by a GW signal is given by [27]

$$H(t) = n_l^i h_{ij}(t) n_l^j, \qquad (5)$$

where $\hat{n}_l$ is the unit vector of the photon propagation. Following Refs. [27, 33], the single arm response to GW
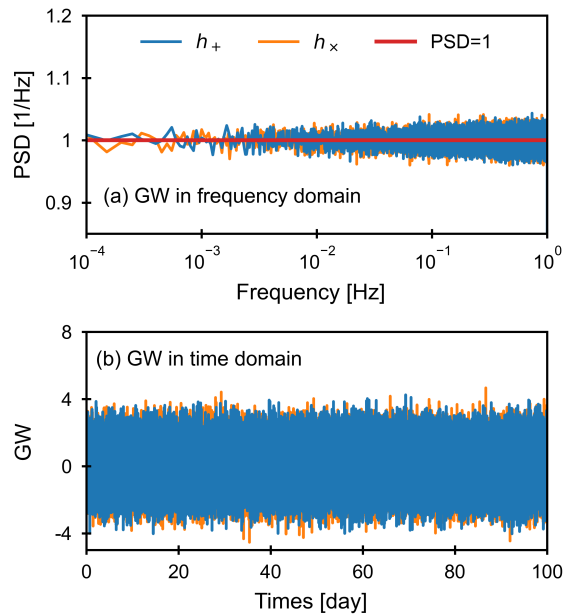

FIG. 3. Simulation for SGWB source configured as a white noise with PSD=1. (a) and (b) are the signals of SGWB in the frequency domain and time domain, respectively. Only the tensor modes are presented in the figure, and the situation is the same for other polarizations.
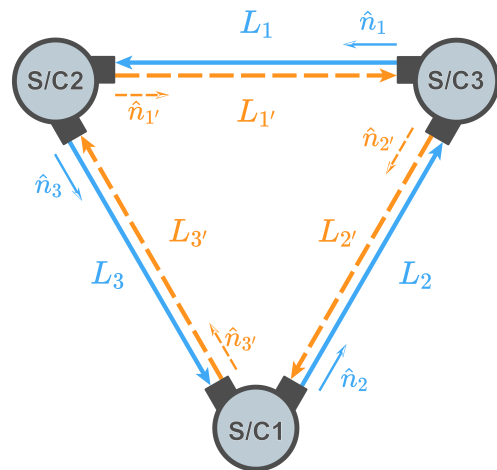

FIG. 4. The constellation of space-based detector.

between S/Ci to S/Cj in time domain can be defined as

$$\eta^{\mathrm{GW}} = \frac{1}{2(1 - \hat{k} \cdot \hat{n}_l)} \left[H(t - \hat{k} \cdot \mathbf{r}_i - L_l) - H(t - \hat{k} \cdot \mathbf{r}_j) \right], \qquad (6)$$

where L_l is the distance of the photon propagation between S/Ci to S/Cj. Some markers and definitions are shown in Figs. 1 and 4. Considering the propagation time of light, the round-trip distances from S/Ci to S/Cj are

not equal, $L_l \neq L_{l'} \neq L$, which are defined as [34]

$$L_1(t) = |\mathbf{r}_2(t-L) - \mathbf{r}_3(t)|, \\ L_{1'}(t) = |\mathbf{r}_3(t-L) - \mathbf{r}_2(t)|. \tag{7}$$

All other L_l can be derived from the cyclical indicators. The unit vector $\hat{n}_l$ is also the same, with $\hat{n}_l \neq -\hat{n}_{l'}$, calculated using the method in Eq. (7).

B. Time-delay interferometry

TDI is a kind of data processing technique, which combines the measurements conducted at different times to realize noise suppression [17]. TDI technique constructs equivalent equal-arm interferometry by combining multiple-link measurements.

TDI technique can be divided into several generations [33]. For the first-generation TDI, in the stationary situation, the arm length is constant in time, with $L_i = L_{i'} = $ const. The modified first-generation TDI, also referred to as TDI-1.5, employ the rigid rotating case, with $L_i = $ const, $L_{i'} = $ const, $L_i \neq L_{i'}$. In the second-generation TDI, a flexing case is adopted, and the arm length is a function of time, with $L_i = L_i(t)$, $L_{i'} = L_{i'}(t)$, $L_i \neq L_{i'}$. In this paper, we adopt the second-generation TDI and conform to the actual situation (see Eq. (7)).

For an arbitrary time-dependent variable $\eta(t)$, a time-delay operator D_i can be defined as

$$D_i\eta(t) = \eta(t-L_i(t)), \\ D_{ji}\eta(t) = \eta(t-L_j(t)-L_i(t-L_j(t))). \tag{8}$$

Then, we can construct various TDI combinations [35]. Here are three typical TDI combinations [36]: the Michelson combination (X,Y,Z), the Sagnac combination (α,β,γ), and the fully symmetric combination (ζ) An important issue is the failure of one laser link, such as a laser source failure. In such case, several TDI combinations that rely on single-link measurements can be used to reconstruct the GW signal [34, 37]. These are called link failure surviving combinations [20]: the Beacon combination (P,Q,R), the Monitor combination (E,F,G), and the Relay combination (U,V,W).

By linearly combining the X,Y,Z channels of the Michelson combination, the so-called optimal combination $(\mathcal{A},\mathcal{E},\mathcal{T})$ can be obtained, defined as [38]

$$\mathcal{A} = \frac{Z-X}{\sqrt{2}}, \ \mathcal{E} = \frac{X-2Y+Z}{\sqrt{6}}, \ \mathcal{T} = \frac{X+Y+Z}{\sqrt{3}}. \tag{9}$$

In an ideal situation, with equal arms and equal noise levels, this combination can eliminate the mutual correlation between signals and noise in different channels [38]. The $\mathcal{T}$ channel is also known as the null channel, which has poor sensitivity in the low-frequency range.

C. Noise and sensitivity

In the payload of space-based detector, there are two optical platforms on each S/C, and each platform outputs three data streams, which contain both GW signals and various noise. By combining these data streams, the application of TDI yields the final datasets corresponding to different channels.
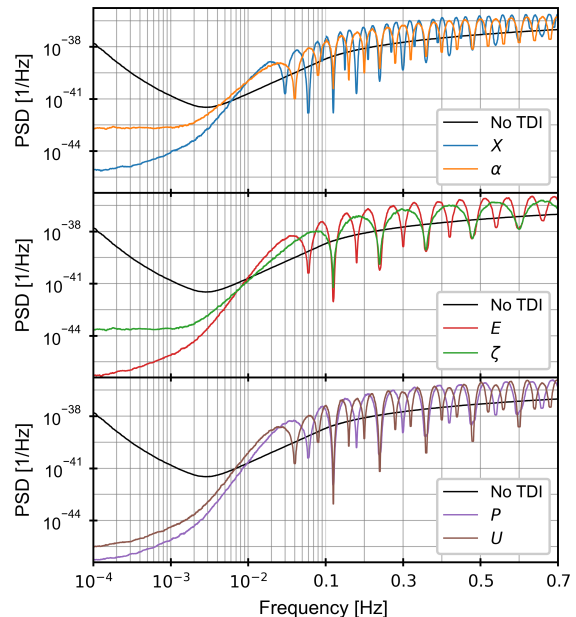

FIG. 5. Noise PSD for different TDI combinations. The part with frequency less than 0.1 Hz uses a logarithmic scale. *No TDI* refers to the interference only between adjacent links, such as $\eta_{31} - \eta_{21}$. Here it is merely for reference since laser frequency noise is not considered. All sensitivity curves and PSD in this paper are numerically simulated. For clarity and conciseness, median smoothing is used.

After TDI technology, laser frequency noise can be suppressed. The instrumental noise of the detector consists of acceleration noise n^{TM} and optical metrology noise n^{OMS} [39, 40]. Neglecting laser frequency noise, the noise terms composed of different data streams can be written as [41, 42]

$$\eta^{\mathrm{Noise}}(t) = n_l^{\mathrm{OMS}}(t) + D_l n_{l'}^{\mathrm{TM}}(t) + n_l^{\mathrm{TM}}(t). \tag{10}$$

Assuming that the instrument noise is Gaussian stationary, the time-domain noise data is generated by transforming the PSD of the frequency-domain noise and adding random phases. Detailed descriptions can be found in Refs. [27, 29, 33]. The data in a single arm can be obtained by independently generating the noise $\eta^{\mathrm{Noise}}(t)$ and GW signal $\eta^{\mathrm{GW}}(t)$ of different links. By employing different TDI combinations, the data $X^{\mathrm{Noise}}(t)$ and $X^{\mathrm{GW}}(t)$ in different channels can be acquired. Such a method can be used to simulate the scenarios of different TDI combinations.

In Fig. 5, the noises processed by different TDI combinations of the second generation are presented. It can be observed that different TDI combinations result in distinct final noise performances. Simply focusing on the PSD of the noise is not sufficient for evaluation, as the GW response is also different for different TDI combinations. One form of evaluating the detector performance is the sensitivity curve. The computation of TDI relies on the polarization angle and sky position of the source, and the sensitivity is calculated using the average of the responses to these parameters. It is typically accomplished through numerical or semi-analytical methods. In this paper, a numerical method is employed to compute the sensitivity curves [43].

The white noise covering the entire frequency band is taken as the response criterion, which is equivalent to the flat SGWB in Sec. II. The polarization angles and sky positions of one hundred sources are uniformly sampled, and the average response is calculated, which is written as

$$R_A = \left\langle \tilde{X}^{\mathrm{GW}}(f) \right\rangle, \tag{11}$$

where $< \cdot >$ represents the average value. Therefore, the sensitivity can be defined as

$$\sqrt{S_n} = \sqrt{P_n/R_A}, \tag{12}$$

where P_n is the PSD of noise. By this approach, the sensitivity curves of different TDI combinations are computed, and they are utilized subsequently for evaluating the performance of the detector and calculating the SNR of different polarizations.

IV. METHODOLOGY

In general, the SNR ρ_A of GW polarization h_A can be defined as

$$\rho_A^2 = (h_A|h_A), \tag{13}$$

where the inner product $(\cdot|\cdot)$ generalizes the time-domain correlation product and is conventionally defined as

$$(a|b) = 4\mathrm{Re}\left[\int_0^\infty \frac{\tilde{a}^*(f)\tilde{b}(f)}{S_n(f)}\mathrm{d}f\right], \tag{14}$$

where $\tilde{a}(f)$ and $\tilde{b}(f)$ are the Fourier transforms of $a(t)$ and $b(t)$, respectively. The overall SNR can be calculated by taking the inner product sum of the SNRs for different polarizations, and it can be expressed as

$$\rho^2 = \sum_A \rho_A^2 = \sum_A (h_A|h_A). \tag{15}$$

Based on such a computational method, we conduct calculations on the simulated data. The simulation and calculation process of this paper is shown in Fig. 6, which can be summarized as follows:
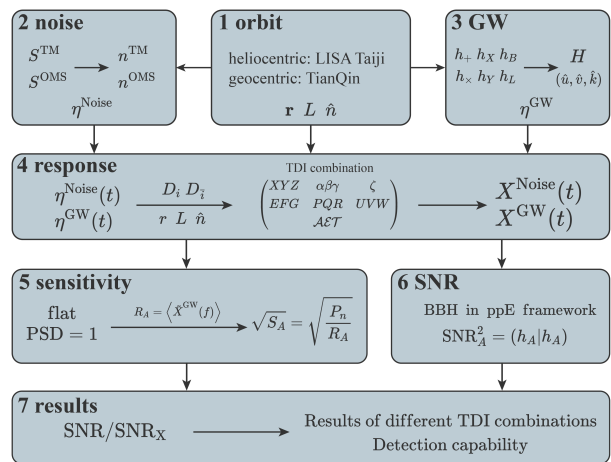

FIG. 6. The flowchart of the simulation and calculation process in this paper.

1. *orbit*: By considering the orbital motions of LISA, Taiji, and TianQin separately, we calculate the light propagation path and direction between the S/C (Sec. III A).

2. *noise*: We compute the time-domain instrument noise from the frequency-domain noise and construct the single-arm noise data stream η^{Noise} (Sec. III C).

3. *GW*: We calculate GW signals from different polarizations, including those from BBH and SGWB, and construct the single-arm GW data stream η^{GW} (Secs. II and III A).

4. *response*: Using various TDI combinations, we simulate the data for both noise and GW signals after TDI processing (Sec. III B).

5. *sensitivity*: Through numerical computation, we calculate the average response and derive the sensitivity curves for different TDI combinations based on these calculations (Sec. III C).

6. *SNR*: We compute the SNR of BBH in the ppE framework for different polarizations (Sec. IV).

7. *results*: We compare the performance of different TDI combinations, evaluating the detection capabilities of different detectors (Sec. V).

In summary, we outline the step-by-step methodology used to simulate and analyze the performance of space-based GW detectors. Next, we present the results of these simulations, comparing the performance of different TDI combinations and analyzing their implications for GW detection.
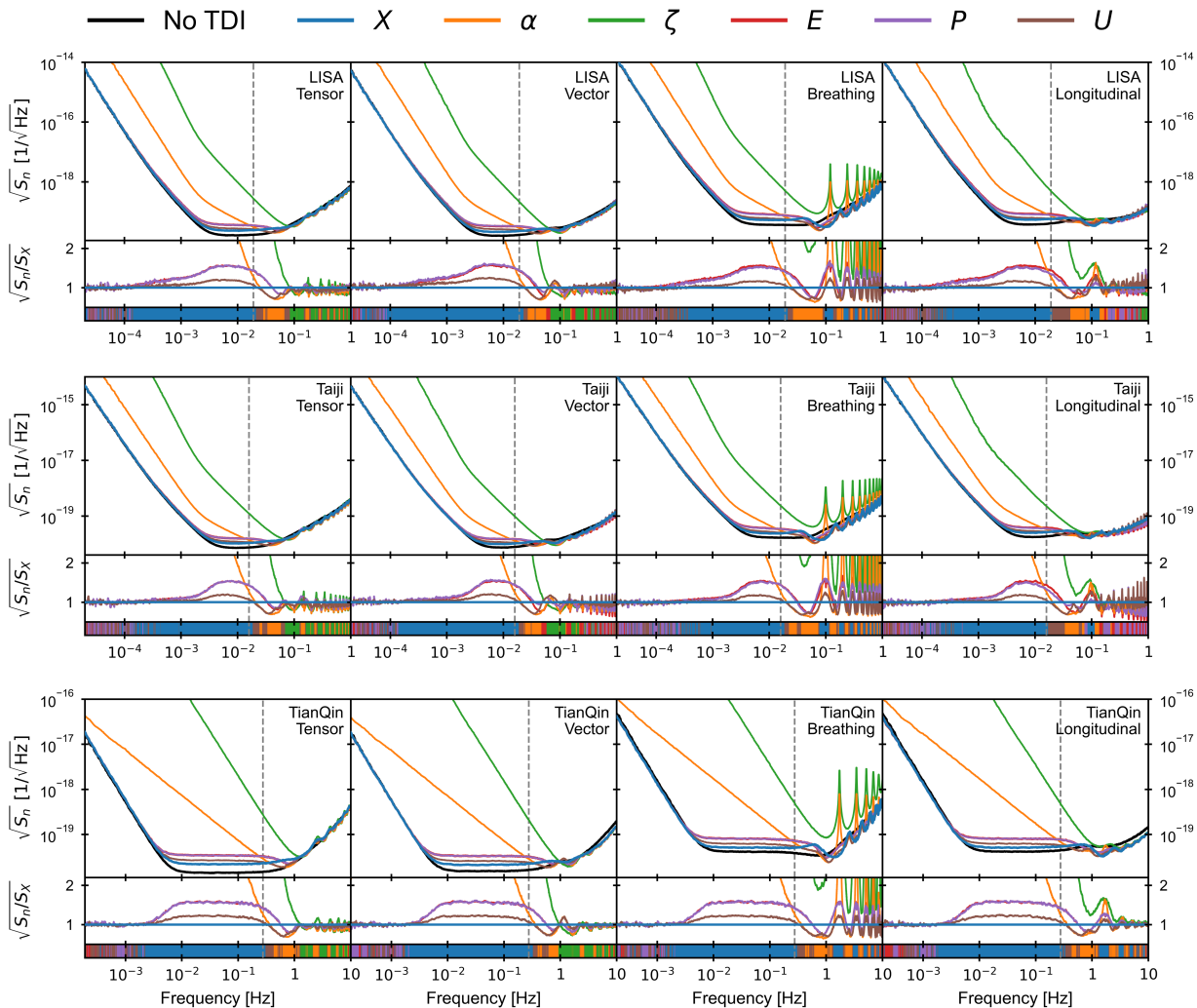
FIG. 7. Comparison of sensitivity curves for various polarizations under different TDI combinations. The sensitivity curves of LISA, Taiji, and TianQin are calculated separately. The second row of each small graph represents the ratio with the X channel as the benchmark. The color bar at the bottom represents the TDI combination with the best sensitivity at that frequency. The vertical-dashed line represents transfer frequency $f_* = 1/(2\pi L)$ [44].

V. RESULTS

A. Constraints on polarization

We simulate and calculate the sensitivity curves in different TDI combinations for different polarizations. The results of LISA, Taiji, and TianQin are shown in Fig. 7.

In general, the lower the sensitivity curve, the better the sensitivity and the stronger the performance of the detector. In the lower frequency range, the sensitivity of the α channel is better than that of the ζ channel. The results of other TDI combinations are regionally consistent and all lower than the former two. In the higher frequency range, the sensitivity curves of the α and ζ channels in the breathing mode present different characteristics. The differences in other TDI combinations or other polarizations are not significant.

In the most sensitive frequency band, the sensitivity curves of different TDI combinations exhibit distinct behaviors. The X channel is the best, followed by the U channel. The E and P channels are nearly the same, both inferior to the X and U channels, and the results of the α and ζ channels are the poorest. Compared with the sensitivity curve without TDI processing, the sensitivity curve after different TDI combinations has a loss in the most sensitive band, although the difference is not significant in the lower and higher frequency bands.

For space-based detectors, the transfer frequency f_* serves as an important dividing line. When the frequency is lower than f_*, the X channel possesses nearly the best sensitivity. When the frequency is higher than f_*, the sensitivity curves of different TDI combinations interlace with each other, and the best TDI combination varies in different frequency bands. Thus, it can be roughly
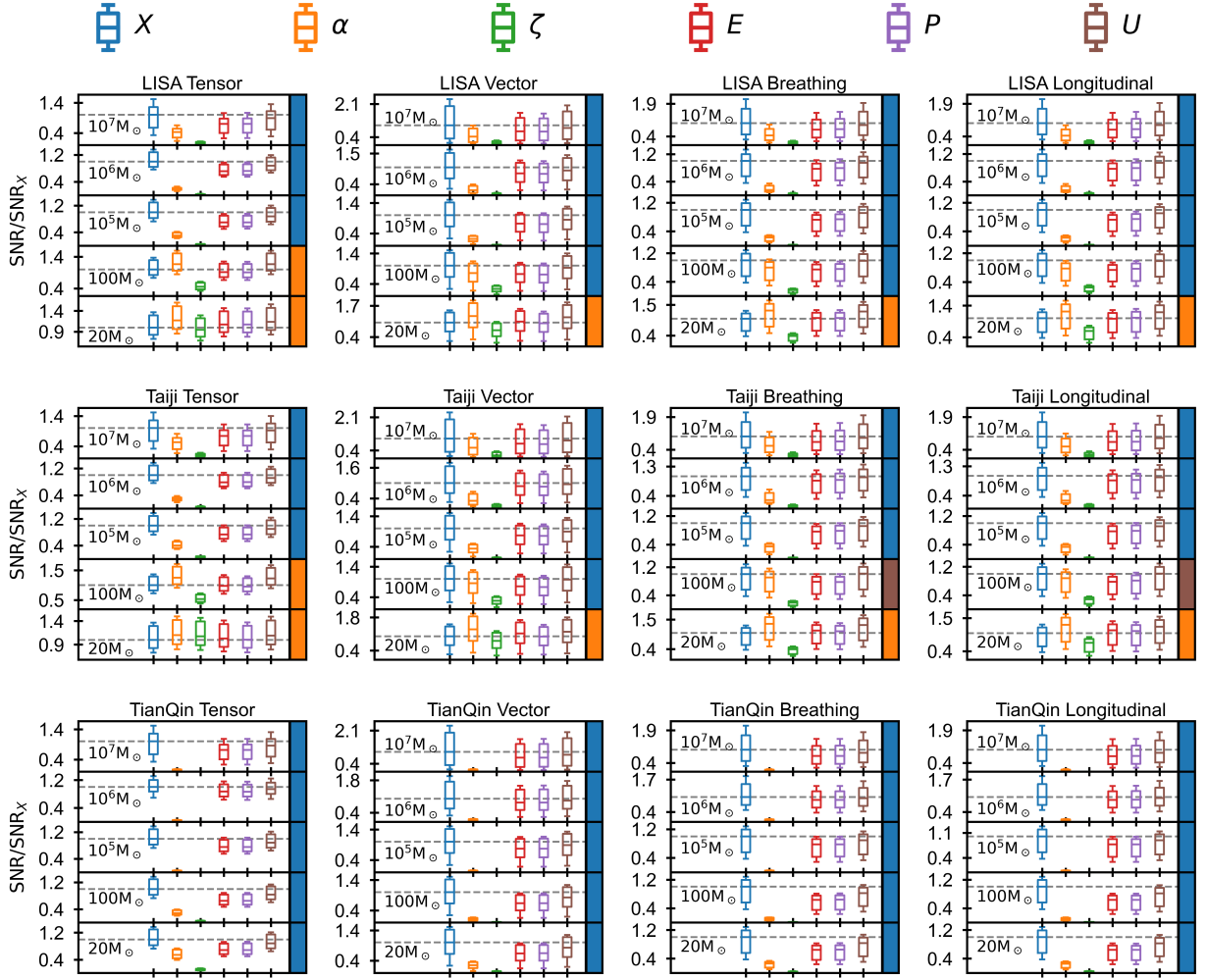
FIG. 8. Comparison of SNR for various polarizations under different TDI combinations. This is the result of using three space-based detectors to detect five different mass BBHs at different sky locations. The upper and lower horizontal lines in each box represent the 90% confidence interval. The edges of the box correspond to the upper and lower quartiles, while the lines inside the box represent the median. The median SNR of the X channel under the same conditions is taken as the benchmark. The color block on the right side of the small graph represents the best TDI combination in this situation.

stated that when the GW signal is in the frequency band lower than f_*, selecting the X channel is the best choice. When it is in the frequency band higher than f_*, the TDI combination should be flexibly chosen in accordance with the characteristics of the signal and the requirements of the analysis. For single-arm damage cases, the U channel has better sensitivity compared with other channels.

To investigate the influences of different TDI combinations on specific GW signals, we simulate the detection of BBH signals. As depicted in Fig. 2, we select these five BBHs with different masses and utilize the sensitivity curve to calculate the SNR with different parameters. The results are presented in Fig. 8.

For MBHB, the SNR of the X channel is the highest because its frequency band is lower than f_*. For SBBH, the results are different. Since part of the SBBH frequency band is lower than f_* of TianQin, the result of

the X channel is still the best for TianQin. Considering LISA and Taiji, the entire frequency band of SBBH is higher than f_*, so the result of the X channel is not necessarily the best. For SBBH with $M = 20$ M$_\odot$, the SNR of the α channel is the highest. For SBBH with $M = 100$ M$_\odot$, the U channel is a suitable choice, even if it is not always the highest, it is very close.

Under the same parametric conditions, the lower the sensitivity curve is, the higher the SNR will be. For the Fisher information matrix, a lower sensitivity curve results in a reduction of the parameter uncertainty [24, 45]. The results in Figs. 7 and 8 can reflect the the ability to constrain on GW polarizations, and a higher SNR corresponds to a smaller parameter uncertainty.

Consequently, in terms of the selected BBHs, when the GW frequency band is lower than f_*, the X channel is the best choice; when the GW frequency band is higher

than f_*, both the α and U channels are excellent options. In the case of single-arm damage and missing data, the U channel is the optimal selection.

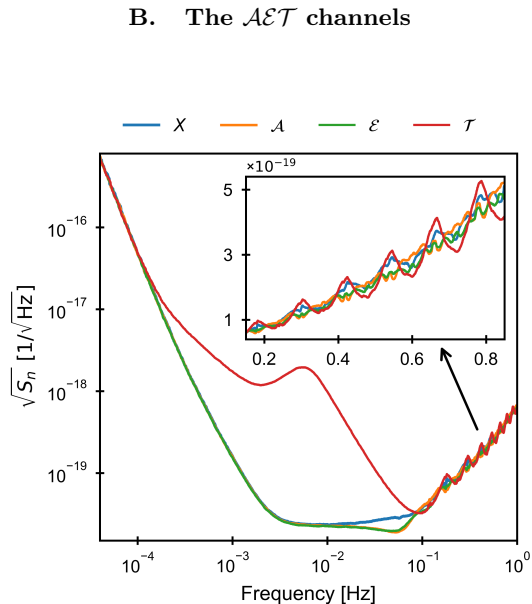## B.   The $\mathcal{AET}$ channels

FIG. 9. Sensitivity curves of the LISA tensor mode.

In the previous section, we compare the influences of different TDI combinations on the sensitivity curve and the SNR of BBH. It could be observed that the X channel is important. Hence, we conduct research on the $\mathcal{AET}$ channels, which are formed by the linear combination of the XYZ channels.

In Fig. 9, the sensitivity curves of the X, $\mathcal{A}$, $\mathcal{E}$, and $\mathcal{T}$ channels in the LISA tensor mode are depicted. As the null channel, the $\mathcal{T}$ channel demonstrates extremely poor sensitivity within the $10^{-4} \sim 10^{-1}$ Hz frequency band, rendering it almost ineffective for signal detection and thereby making it a favorable monitor for certain noises. In the frequency band greater than 0.1 Hz, the $\mathcal{T}$ channel undergoes more significant fluctuations compared to the other channels. The $\mathcal{A}$ and $\mathcal{E}$ channels are highly similar and slightly outperform the X channel in the most sensitive frequency band, particularly in the $10^{-2} \sim 10^{-1}$ Hz frequency band.

We employ the research approach from the previous section to assess the performance by computing the SNR of BBHs with five different masses. The SNR results of the three detectors with different polarizations are presented in Fig. 10.

For LISA and Taiji, apart from the $\mathcal{T}$ channel, the differences between the X, $\mathcal{A}$, and $\mathcal{E}$ channels are negligible. Since the sensitivity curves of these channels are highly proximate at low frequencies, the SNR results of MBHB are almost the same. In most cases, the results of the $\mathcal{A}$ and $\mathcal{E}$ channels are slightly better than those of the X channel. Regarding SBBH, due to the difference in the
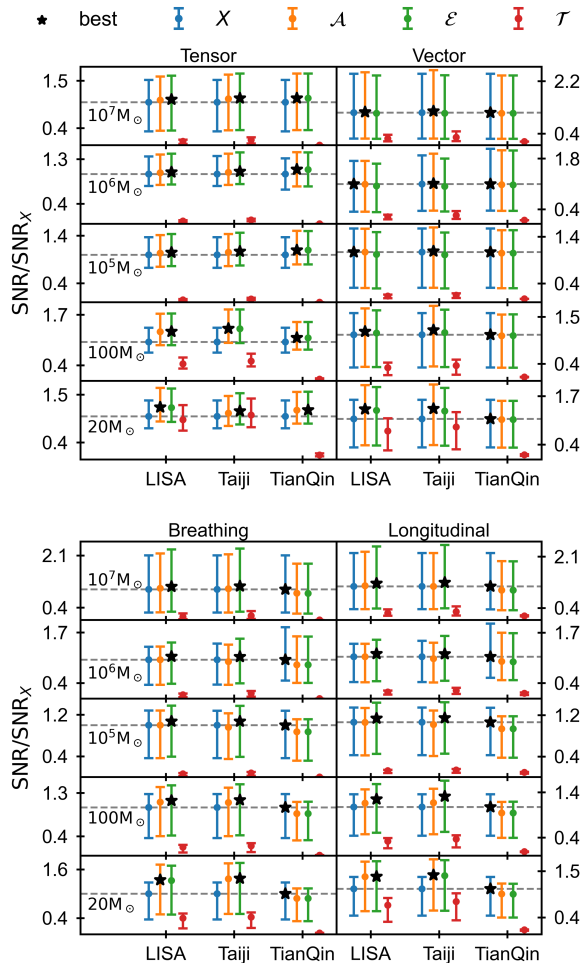

FIG. 10. Comparison of SNR for various polarizations under Michelson and optimal combinations. For simplicity, we use points to represent the median, with error bars above and below indicating the 90% confidence interval. The black stars represent the best channels.

most sensitive frequency band, the SNR of the $\mathcal{A}$ and $\mathcal{E}$ channels exhibits a marked improvement compared to that of the X channel. Even in the tensor mode, for the SBBH with $M = 20$ $M_\odot$, the SNR of the $\mathcal{T}$ channel can attain the same level as that of the X channel.

For TianQin, the difference in the sensitive frequency band range leads to different results compared with LISA and Taiji. In the tensor mode, the results of the $\mathcal{A}$ and $\mathcal{E}$ channels are slightly better than those of the X channel. Among the remaining polarizations, judging from the final results, the X channel turns out to be the best. Nevertheless, in the vector mode, the results of the X, $\mathcal{A}$, and $\mathcal{E}$ channels are almost the same, while in the breathing and longitudinal modes, the SNR of the X channel is conspicuously higher than that of the $\mathcal{A}$ and $\mathcal{E}$ channels. Additionally, in all polarizations, the $\mathcal{T}$ channel is almost unusable.

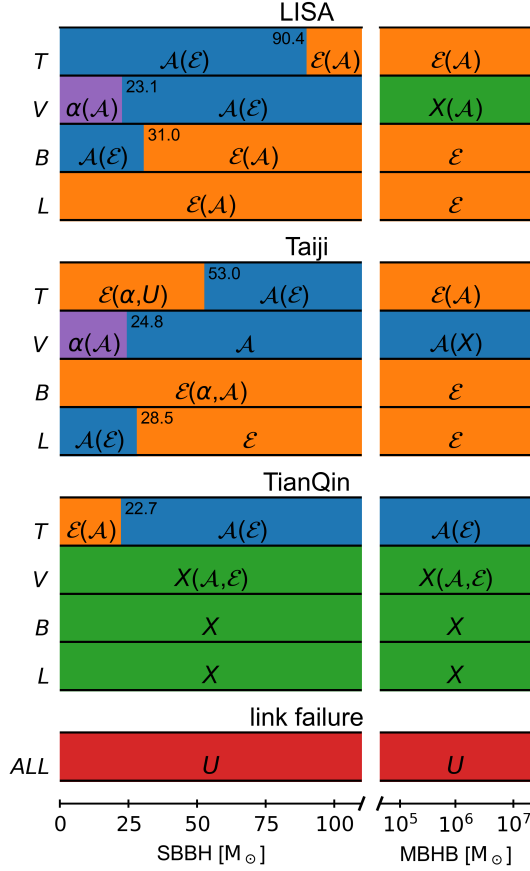Overall, for different space-based detectors detecting

FIG. 11. The best channel selection for detecting different polarizations using SBBH and MBHB. The content before the parentheses represents the best channel in the corresponding situation, and the content within the parentheses indicates the excellent channels, with a deviation of within 3% from the best channel. The numbers signify the demarcation lines for choosing different channels in the SBBH detection. The left-hand side *T, V, B, L* stands for tensor, vector, breathing, and longitudinal modes, while *ALL* stands for all polarizations.

BBHs with different masses, the best TDI combinations are different. The specific choices are listed in Fig. 11. Regarding MBHB, for different detectors to detect different polarizations, there is a sole optimal choice. As for SBBH, the best channel needs to be selected based on the mass. Under most circumstances, the X channel and the $\mathcal{A}, \mathcal{E}$ channels constructed from it have the most powerful performance. For LISA and Taiji detecting the vector mode of small-mass SBBH, the result of the α channel is superior to the other channels. When one laser link is damaged, the U channel is always the best choice for detecting BBH with any polarization and any mass.

C. Detection capability

Considering the influence brought by different TDI combinations, in addition to the study of different po-
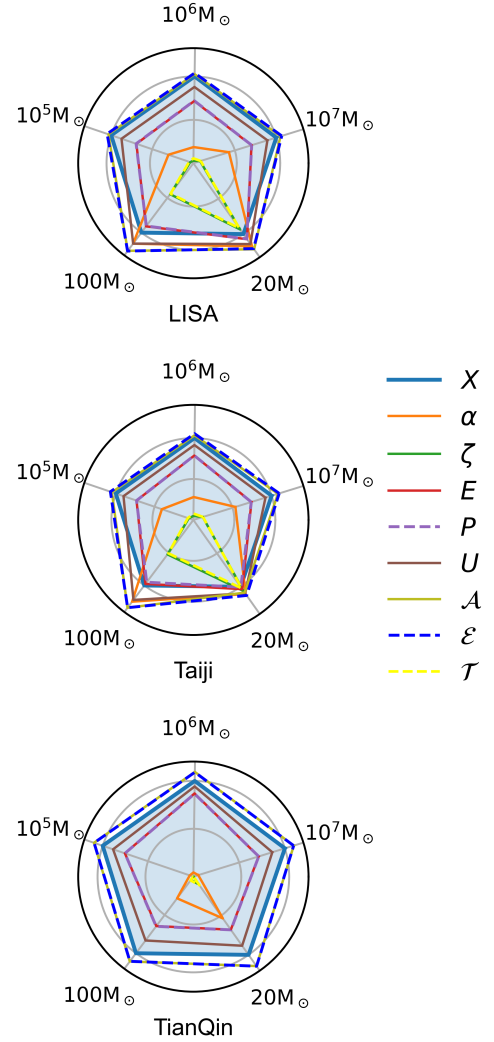

FIG. 12. Comparison of detection capability for various polarizations under different TDI combinations. The detection capability of the X channel is taken as the benchmark. The further out the line, the greater the detection ability.

larizations, the detection capability is also of great significance. The detection capability is measured by calculating the total SNR under different parameters. The results of five BBHs with different masses under various parameters and using different TDI combinations are presented as shown in Fig. 12.

For LISA and Taiji, their orbital configurations are similar, thereby yielding similar results. In the detection of MBHB, the results of the $\mathcal{A}$ and $\mathcal{E}$ channels are identical and marginally superior to that of the X channel, while the other channels are inferior to the X channel. In the detection of SBBH, the $\mathcal{A}$ and $\mathcal{E}$ channels have the strongest detection ability, and the α and U channels surpass the X channel. For SBBH with even lower mass, the E and P channels even exceed the X channel, and the detection capabilities of the ζ and $\mathcal{T}$ channels have

also increased.

For TianQin, the difference in its frequency band results to similar results in detecting MBHB and SBBH. The detection capabilities of the $\mathcal{A}$ and $\mathcal{E}$ channels are identical and the strongest in all circumstances. The result of the X channel comes next, and the result of the U channel is lower than that of the X channel. The E and P channels have the same detection capabilities, as do the ζ and $\mathcal{T}$ channels. Additionally, as the mass of BBH decreases, the results of the α, ζ and $\mathcal{T}$ channels improve.

In conclusion, in terms of detection capabilities, the $\mathcal{A}$ and $\mathcal{E}$ channels are the best in all respects. The X channel remains a very good option in most cases, especially for MBHB. When detecting SBBH with LISA and Taiji, choosing the α and U channels is appropriate. In the E, P and U channels, if there is a failure that leads to data loss, the U channel is the best choice.

VI.   CONCLUSION

In this paper, we investigate the constraints and detection capabilities of GW polarization with space-based GW detectors in different TDI combinations. Specifically, for space-based detectors, we take into account the orbital configurations of LISA, Taiji, and TianQin. Considering the possible circumstances that might occur in reality, seven different second-generation TDI combinations are simulated. We conduct simulations of both GW signals and instrument noise separately. The average response is calculated through the flat-spectrum SGWB to obtain the sensitivity curve. Utilizing GW waveforms encompassing six polarizations in the ppE framework and considering five different masses of BBH, the SNR for various parameter conditions is calculated. By employing such methods, we calculate and analyze the influences of different TDI combinations on the constraints and detection capabilities of GW polarizations.

Our research indicates that for the fundamental six TDI combinations, the X channel exhibits superior sensitivity when the frequency is less than f_*. When the frequency exceeds f_*, a flexible choice is necessary. In the case of single-arm data loss, the U channel demon-strates better sensitivity. For MBHB, the SNR of the X channel is the highest. For SBBH, the use of the α or U channel is more favorable in LISA and Taiji, while Tian-Qin still performs best with the X channel. Considering the $\mathcal{AET}$ channels constructed from the linear combination of the XYZ channels, both the $\mathcal{A}$ and $\mathcal{E}$ channels are excellent options in LISA and Taiji. For TianQin, the $\mathcal{A}$ and $\mathcal{E}$ channels are only optimal for the tensor mode, while for additional polarizations, the X channel is still superior.

Regarding the detection ability, $\mathcal{A}$ and $\mathcal{E}$ channels are the best, outperforming other TDI combinations. In the remaining TDI combinations, the X channel is excellent for detecting MBHB. For detecting SBBH with LISA and Taiji, the detection capabilities of α and U channels are better, yet the X channel is still the best with TianQin. When detecting SBBH of smaller masses, E and P channels with LISA and Taiji even surpass the X channel, and the detection capabilities of ζ and $\mathcal{T}$ channels are also close to that of the X channel. Moreover, if one link is damaged, the U channel has the best detection ability.

In future research, we plan to explore a range of TDI combinations to assess their impact on various GW signals, including different SGWB signals. By incorporating these diverse TDI techniques, we aim to enhance the thoroughness of our study and achieve more realistic, robust results. This expanded approach will not only provide a more comprehensive analysis of the detection capabilities of space-based GW detectors but also improve our ability to search for alternative polarization modes, offering a deeper test of GR. Ultimately, our research will contribute valuable insights into the performance of different TDI combinations and advancing the detection of GW across different detectors.

[1] B. P. Abbott *et al.* (LIGO Scientific, Virgo), Observation of Gravitational Waves from a Binary Black Hole Merger, Phys. Rev. Lett. **116**, 061102 (2016), arXiv:1602.03837 [gr-qc].

[2] C. Shi, M. Ji, J.-d. Zhang, and J. Mei, Testing general relativity with TianQin: The prospect of using the inspiral signals of black hole binaries, Phys. Rev. D **108**, 024030 (2023), arXiv:2210.13006 [gr-qc].

[3] B. P. Abbott *et al.* (LIGO Scientific, Virgo), Tests of General Relativity with the Binary Black Hole Signals from the LIGO-Virgo Catalog GWTC-1, Phys. Rev. D **100**, 104036 (2019), arXiv:1903.04467 [gr-qc].

[4] R. Abbott *et al.* (LIGO Scientific, Virgo), Tests of general relativity with binary black holes from the second LIGO-Virgo gravitational-wave transient catalog, Phys. Rev. D **103**, 122002 (2021), arXiv:2010.14529 [gr-qc].

[5] R. Abbott *et al.* (LIGO Scientific, VIRGO, KAGRA), Tests of General Relativity with GWTC-3 (2021), arXiv:2112.06861 [gr-qc].

[6] J. Aasi *et al.* (LIGO Scientific), Advanced LIGO, Class. Quant. Grav. **32**, 074001 (2015), arXiv:1411.4547 [gr-qc].

[7] F. Acernese *et al.* (VIRGO), Advanced Virgo: a second-

generation interferometric gravitational wave detector, Class. Quant. Grav. **32**, 024001 (2015), arXiv:1408.3978 [gr-qc].

[8] K. Somiya (KAGRA), Detector configuration of KAGRA: The Japanese cryogenic gravitational-wave detector, Class. Quant. Grav. **29**, 124007 (2012), arXiv:1111.7185 [gr-qc].

[9] R.-G. Cai, Z.-K. Guo, B. Hu, C. Liu, Y. Lu, W.-T. Ni, W.-H. Ruan, N. Seto, G. Wang, and Y.-L. Wu, On networks of space-based gravitational-wave detectors (2023), arXiv:2305.04551 [gr-qc].

[10] J. Wu and J. Li, Subtraction of the confusion foreground and parameter uncertainty of resolvable galactic binaries on the networks of space-based gravitational-wave detectors, Phys. Rev. D **108**, 124047 (2023), arXiv:2307.05568 [gr-qc].

[11] P. Amaro-Seoane, H. Audley, S. Babak, J. Baker, E. Barausse, P. Bender, E. Berti, P. Binetruy, M. Born, D. Bortoluzzi, *et al.*, Laser interferometer space antenna (2017), arXiv:1702.00786 [astro-ph.IM].

[12] W.-R. Hu and Y.-L. Wu, The Taiji Program in Space for gravitational wave physics and the nature of gravity, Natl. Sci. Rev. **4**, 685 (2017).

[13] J. Luo *et al.* (TianQin), TianQin: a space-borne gravitational wave detector, Class. Quant. Grav. **33**, 035010 (2016), arXiv:1512.02076 [astro-ph.IM].

[14] S. Kawamura *et al.*, The Japanese space gravitational wave antenna: DECIGO, Class. Quant. Grav. **28**, 094011 (2011).

[15] J. Crowder and N. J. Cornish, Beyond LISA: Exploring future gravitational wave missions, Phys. Rev. D **72**, 083005 (2005), arXiv:gr-qc/0506015.

[16] C. Cutler and J. Harms, BBO and the neutron-star-binary subtraction problem, Phys. Rev. D **73**, 042001 (2006), arXiv:gr-qc/0511092.

[17] M. Tinto and S. V. Dhurandhar, Time-delay interferometry, Living Rev. Rel. **24**, 1 (2021).

[18] M. Tinto and J. W. Armstrong, Cancellation of laser noise in an unequal-arm interferometer detector of gravitational radiation, Phys. Rev. D **59**, 102003 (1999).

[19] C. Zhang, Q. Gao, Y. Gong, D. Liang, A. J. Weinstein, and C. Zhang, Frequency response of time-delay interferometry for space-based gravitational wave antenna, Phys. Rev. D **100**, 064033 (2019), arXiv:1906.10901 [gr-qc].

[20] M. Tinto, F. B. Estabrook, and J. W. Armstrong, Time delay interferometry with moving spacecraft arrays, Phys. Rev. D **69**, 082001 (2004), arXiv:gr-qc/0310017.

[21] Z.-Q. Wu, P.-P. Wang, W.-L. Qian, and C.-G. Shao, Combinatorial algebraic approach for modified second-generation time-delay interferometry, Phys. Rev. D **107**, 024042 (2023), arXiv:2210.07801 [astro-ph.IM].

[22] P.-P. Wang, Y.-J. Tan, W.-L. Qian, and C.-G. Shao, Sensitivity functions of space-borne gravitational wave detectors for arbitrary time-delay interferometry combinations regarding nontensorial polarizations, Phys. Rev. D **104**, 023002 (2021).

[23] G. Wang, W.-T. Ni, W.-B. Han, and C.-F. Qiao, Algorithm for time-delay interferometry numerical simulation and sensitivity investigation, Phys. Rev. D **103**, 122006 (2021), arXiv:2010.15544 [gr-qc].

[24] J. Wu and J. Li, Prospects of constraining on the polarizations of gravitational waves from binary black holes using space- and ground-based detectors (2024), arXiv:2407.13590 [gr-qc].

[25] J. Wu, J. Li, X. Liu, and Z. Cao, Comparison and application of different post-Newtonian models for inspiralling stellar-mass binary black holes with space-based GW detectors, Phys. Rev. D **109**, 104014 (2024), arXiv:2401.03113 [gr-qc].

[26] C. Liu, W.-H. Ruan, and Z.-K. Guo, Constraining gravitational-wave polarizations with Taiji, Phys. Rev. D **102**, 124050 (2020), arXiv:2006.04413 [gr-qc].

[27] E.-K. Li, H. Wang, H.-Y. Chen, H. Fan, Y.-N. Li, Z.-Y. Li, Z.-C. Liang, X.-Y. Lyu, T.-X. Wang, Z. Wu, C.-Q. Ye, X.-T. Zhang, Y. Hu, and J. Mei, Gwspace: a multi-mission science data simulator for space-based gravitational wave detection (2023), arXiv:2309.15020 [gr-qc].

[28] L. O'Beirne, N. J. Cornish, S. J. Vigeland, and S. R. Taylor, Constraining alternative polarization states of gravitational waves from individual black hole binaries using pulsar timing arrays, Phys. Rev. D **99**, 124039 (2019), arXiv:1904.02744 [gr-qc].

[29] T. Robson, N. J. Cornish, and C. Liu, The construction and use of LISA sensitivity curves, Class. Quant. Grav. **36**, 105011 (2019), arXiv:1803.01944 [astro-ph.HE].

[30] S. Babak, M. Hewitson, and A. Petiteau, Lisa sensitivity and snr calculations (2021), arXiv:2108.01167 [astro-ph.IM].

[31] B. Wu, C.-G. Huang, and C.-F. Qiao, Analytical analysis on the orbits of Taiji spacecrafts, Phys. Rev. D **100**, 122001 (2019), arXiv:1907.06178 [gr-qc].

[32] X.-C. Hu, X.-H. Li, Y. Wang, W.-F. Feng, M.-Y. Zhou, Y.-M. Hu, S.-C. Hu, J.-W. Mei, and C.-G. Shao, Fundamentals of the orbit and response for TianQin, Class. Quant. Grav. **35**, 095008 (2018), arXiv:1803.03368 [gr-qc].

[33] Z. Ren, T. Zhao, Z. Cao, Z.-K. Guo, W.-B. Han, H.-B. Jin, and Y.-L. Wu, Taiji data challenge for exploring gravitational wave universe, Front. Phys. (Beijing) **18**, 64302 (2023), arXiv:2301.02967 [gr-qc].

[34] M. Otto, *Time-Delay Interferometry Simulations for the Laser Interferometer Space Antenna*, Ph.D. thesis, Leibniz U., Hannover (2015).

[35] F. B. Estabrook, M. Tinto, and J. W. Armstrong, Time delay analysis of LISA gravitational wave data: Elimination of spacecraft motion effects, Phys. Rev. D **62**, 042002 (2000).

[36] J. W. Armstrong, F. B. Estabrook, and M. Tinto, Time-delay interferometry for space-based gravitational wave searches, The Astrophysical Journal **527**, 814 (1999).

[37] A. Chou *et al.* (Holometer), The Holometer: An Instrument to Probe Planckian Quantum Geometry, Class. Quant. Grav. **34**, 065005 (2017), arXiv:1611.08265 [physics.ins-det].

[38] T. A. Prince, M. Tinto, S. L. Larson, and J. W. Armstrong, The LISA optimal sensitivity, Phys. Rev. D **66**, 122002 (2002), arXiv:gr-qc/0209039.

[39] M. Tinto and O. Hartwig, Time-Delay Interferometry and Clock-Noise Calibration, Phys. Rev. D **98**, 042003 (2018), arXiv:1807.02594 [gr-qc].

[40] J.-B. Bayle, M. Lilley, A. Petiteau, and H. Halloin, Effect of filters on the time-delay interferometry residual laser noise for LISA, Phys. Rev. D **99**, 084023 (2019), arXiv:1811.01575 [astro-ph.IM].

[41] G. Wang, Satdi: Simulation and analysis for time-delay interferometry (2024), arXiv:2403.01726 [gr-qc].

[42] J. Alvey, U. Bhardwaj, V. Domcke, M. Pieroni, and C. Weniger, Leveraging time-dependent instrumental

noise for lisa sgwb analysis (2024), arXiv:2408.00832 [gr-qc].

[43] S. Babak, A. Petiteau, and M. Hewitson, LISA Sensitivity and SNR Calculations (2021), arXiv:2108.01167 [astro-ph.IM].

[44] N. J. Cornish and S. L. Larson, Space missions to detect the cosmic gravitational wave background, Class. Quant. Grav. **18**, 3473 (2001), arXiv:gr-qc/0103075.

[45] M. Vallisneri, Use and abuse of the Fisher information matrix in the assessment of gravitational-wave parameter-estimation prospects, Phys. Rev. D **77**, 042001 (2008), arXiv:gr-qc/0703086.